Wang et al. J Mater. Sci: Mater Eng. (2025) 20:31
https://doi.org/10.1186/s40712-025-00235-6

Journal of Materials Science: Materials in Engineering

ORIGINAL PAPER

Open Access

Preparation of high-performance Ag_2Se NWs/PEDOT:PSS composite films and influence of PEDOT:PSS content on thermoelectric properties

Ruoxi Wang[1], Rongke Sun[1], Yanmei Ren[1], Yanqing Ma[1,2,3*] and Lei Ma[1,2*]

Abstract

There is still limited research on the influence of polymer content in inorganic/organic materials on thermoelectric properties. In this study, we systematically investigated the influence of the content of poly(3,4-ethylenedioxythiophene):poly(styrenesulfonate) (PEDOT:PSS) in the Ag_2Se nanowires/PEDOT:PSS (Ag_2Se NWs/PEDOT:PSS) composite films on the thermoelectric properties. When the content of PEDOT:PSS is 1.54 wt%, the composite film achieved the highest power factor (PF) of ~ 2074.0 μW m^{-1} K^{-2} at room temperature. The maximum output power (P_{max}) of the single-leg thermoelectric device based on the composite film is approximately 49.42 nW, and the maximum power density (PD_{max}) is 4.28 W m^{-2} at a temperature difference of 25 K. Furthermore, the film exhibits superior flexibility with 94.3% of the original performance retention after 2000 bending cycles around a rod with a diameter of 5 mm. This work provides valuable guidance for the design and fabrication of high-performance flexible inorganic/organic composite thermoelectric materials.

Keywords Ag_2Se NWs, PEDOT:PSS, Inorganic/organic composites, Flexible, Thermoelectric materials

Introduction

In recent years, the demand for flexible, portable, and wearable electronic devices has greatly stimulated the development of environmentally friendly power sources (Sun et al. 2022; Huang et al. 2022; Xu et al. 2019). Flexible thermoelectric materials and devices can realize the direct conversion of thermal and electricity, and vice versa. They have the advantages of long service life, good stability, and no noise and thus have vast research prospects in the field of energy harvest and sensor (Shi et al. 2020; Zhang et al. 2021a; Wang et al. 2019). However, achieving both good flexibility and excellent thermoelectric properties simultaneously remains a bottleneck in the development of flexible thermoelectric materials and devices.

Low-dimensional materials/polymer composite materials have a wide prospect in the field of flexible thermoelectric, which combines the advantages of the high Seebeck coefficient of low-dimensional inorganic materials and the high flexibility and low thermal conductivity of conductive polymers (Liu et al. 2021a). P-type low-dimensional materials/polymer composite thermoelectric materials have been extensively studied and exhibit excellent thermoelectric properties (Du et al. 2014; Ren et al. 2023; Zhang et al. 2021b). Improving the

*Correspondence:
Yanqing Ma
mayanqing@tju.edu.cn
Lei Ma
lei.ma@tju.edu.cn
[1] Tianjin International Center for Nanoparticles and Nanosystems, Tianjin University, Tianjin 300072, People's Republic of China
[2] Tianjin Key Laboratory of Low-Dimensional Electronic Materials and Advanced Instrumentation, Tianjin 300072, People's Republic of China
[3] School of Precision Instrument and Opto-Electronics Engineering, Tianjin University, Tianjin 300072, People's Republic of China

thermoelectric properties of corresponding n-type low-dimensional materials/polymer composites is of significant value for the practical application of thermoelectric devices (Lu et al. 2024). The proportion of components plays an important role in improving the thermoelectric properties of n-type composites. Ji Young Jo prepared a series of Bi_2Te_3/PEDOT:PSS composite thin films with different content of n-Bi_2Te_3. The thermoelectric properties of the composites are enhanced through the creation of additional defects in n-Bi_2Te_3 via proton irradiation. A maximum power factor of 328 ± 48 μW m^{-1} K^{-2} is obtained for the Bi_2Te_3/PEDOT:PSS composite films with the concentration of Bi_2Te_3 at 0.5 wt% irradiated using proton energy of ≥ 12 MeV (Goo et al. 2019). However, the thermoelectric properties of n-type low-dimensional materials/polymers composite materials are still at a low level, which limits the practical application of the thermoelectric devices. Ag_2Se NWs are easier to prepare and chemically stable at room temperature compared to Bi_2Te_3 NWs. It exhibits excellent thermoelectric properties, which is considered to be a promising thermoelectric material near room temperature (Jiang et al. 2020; Liu et al. 2023; Hu et al. 2024; Yang et al. 2024). Prof. Cai's group prepared the Ag_2Se/Se/PPy composite films that showed improved Seebeck coefficient and conductivity when the amount of PPy was 1 μL. The power factor of the composite film at 300 K is about 2240 μW m^{-1} K^{-2} (Li et al. 2022). Compared to PPy, PEDOT:PSS has good dispersion in water and easy solution process. It can provide more conductive pathways in composite materials, which helps to achieve the optimization of thermoelectric properties (Zhou et al. 2021). Ag_2Se NWs/PEDOT:PSS composites demonstrate great potential in achieving excellent thermoelectric properties (Meng et al. 2024).

In this paper, Ag_2Se NWs/PEDOT:PSS composite materials were prepared through simple physical mixing. The content of PEDOT:PSS was systematically regulated to obtain the improved thermoelectric properties of Ag_2Se NWs/PEDOT:PSS composites. When the content of PEDOT:PSS is 1.54 wt%, the composites have the most excellent power factor that is ~ 2074.0 μW m^{-1} K^{-2}. The energy filtration effect between the interface of Ag_2Se NWs and PEDOT:PSS was researched by KPFM. This work provides valuable guidance for the design and fabrication of high-performance flexible composite thermoelectric materials and devices.

Experimental section

Materials

The materials are SeO_2 (99%, Shanghai Aladdin Biochemical Technology Co., LTD), β-cyclodextrin (98%, Tianjin Heowns Biochemical Technology Co., LTD), ascorbic acid (99.7%, Tianjin Fengchuan Chemical reagent Co., LTD), ethylene glycol (98%, Heowns Biochem Technologies, LLC, Tianjin), $AgNO_3$ (99.9%, Shanghai Fine Chemical Materials Research Institute), and PEDOT:PSS (1.3 wt%, Heowns Biochem Technologies, LLC, Tianjin). All these materials were used as received without further processing unless otherwise specified.

Preparation of Se NWs and Ag_2Se NWs

Preparation of Se NWs

A 0.5 g of SeO_2 and 0.5 g of β-cyclodextrin were added to 100 mL of deionized water and stirred for 10 min to form solution A. Two grams of ascorbic acid and 100 mL of deionized water were added and stirred for 10 min to form solution B. Under continuous stirring, solution A was slowly added dropwise into solution B. The color of the mixed solution rapidly changed from colorless to yellow and immediately to brick red. After 4 h of reaction at room temperature, the resulting precipitate was collected by centrifugation. The centrifugation was performed at 11,000 rpm for 10 min, and the precipitate was washed four times with deionized water and ethanol alternately. The washed final precipitate was stored in 100 mL of anhydrous ethanol and allowed to settle at room temperature for 48 h. During this process, the color of the solution changed from brick red to dark red, and flocculent precipitates formed. The collected precipitate was dried in at vacuum oven at 40 °C for 12 h to obtain the powder of Se NWs (Li and Yam 2006) (Fig. S1).

Preparation of Ag_2Se NWs

A 0.5 g of Se NWs was dispersed in 50 mL of ethanol and vigorously stirred to form a well-dispersed solution. Then, 0.43 g of $AgNO_3$ was slowly added to the solution. The mixture was stirred for 2 h at 40 °C, followed by centrifugation to collect the product. The following reactions occurred during the synthesis of Ag_2Se NWs (Park et al. 2021a):

$$2Ag^{+} + C6H8O6 \rightarrow 2Ag + C6H6O6 + 2H^{+} \quad (1)$$

$$2Ag + Se \rightarrow Ag2Se \quad (2)$$

The collected product was washed four times with deionized water and ethanol alternately. Finally, the product was dried in at vacuum oven at 50 °C for 4 h to obtain the powder of Ag_2Se NWs (Ding et al. 2019).

Preparation of Ag_2Se NWs/PEDOT:PSS composite films

Five milligrams of Ag_2Se NWs was dispersed in 10 mL of ethanol and sonicated at 28 kHz for 30 min to obtain a well-dispersed solution. Then, 1, 3, 6, 9, 12, 20, and 45 μL of a 1.3 wt% aqueous solution of PEDOT:PSS were separately added to the solution. The mixture was

sonicated at 28 kHz for 30 min to ensure uniform dispersion. Finally, the Ag_2Se NWs/PEDOT:PSS composite films with different mass fractions of PEDOT:PSS were obtained by vacuum filtration on a nylon membrane with a diameter of 25 mm and pore size of 0.22 μm. The composite films were dried in at vacuum oven at 50 °C for 4 h and cold pressed at 10 MPa for 10 min to obtain the final flexible composite films (Fig. 1). The composite samples were named AP*x*, and the "*x*" represents the volume of PEDOT:PSS added. The pure Ag_2Se NWs sample was named AP0. The corresponding PEDOT:PSS mass fractions in the composites were 0, 0.26, 0.77, 1.54, 2.29, 3.03, 4.94, and 10.47 wt%, respectively. After cold pressing, it was difficult to separate the composite from the nylon film, so the final composite did not peel off from the nylon substrate.

Characterizations

The surface morphology of samples was characterized by scanning electron microscope (SEM, Hitachi, SU-3500). The energy dispersive X-ray spectroscopy (EDS, IXRF SYSTEM, SU-3500) was used to characterize the element components and distribution of materials. X-ray diffractometer (XRD, TD3500, Cu Kα, $\lambda = 0.154$ nm) and X-ray photoelectron spectroscopy (XPS, Perkin-Elmer, PHI 5100) were used to analyze the crystal structure and their chemical composition. The work function of Ag_2Se NWs and PEDOT:PSS were measured by Kelvin Probe Force Microscopy (KPFM, Park, NX10). The Seebeck coefficient of the thermoelectric films was characterized by a homemade test system, in which the heat source was PI heating film. The potential signal and temperature signal were respectively collected by a digital multimeter (Keysight, 34461A) and digital thermocouple (K, UNI-T, UT320A). The conductivity of the materials was characterized by a four-probe tester (C-4, EVERBEING) and a digital source meter (Keithley, 2612B). The response electrical signals of flexible thermoelectric devices were collected by a digital multimeter (Keysight, 34461A).

Results and discussions

Figure 2(a) shows the surface SEM image of Se NWs. It can be seen that the Se NWs are about 150 nm in diameter and about 5 μm in length. EDS mapping and spectra of Se NWs show the main element is Se in the Se NWs (Fig. S2(a)–(c)). All diffraction peaks corresponding to the pure hexagonal phase structure of Se, with lattice parameters of $a = 4.37$ Å and $c = 4.95$ Å (JCPDS 06–0362), indicating that the Se NWs grow preferentially along the (101) crystal face due to orientation effect (Fig. 2(b)). As shown in Fig. 2(c), Ag_2Se NWs have a similar one-dimensional (1D) nanowire morphology to that of Se NWs, but the length (~4 μm) is slightly smaller than Se NWs. It may be caused by the fragmentation of the one-dimensional nanostructure during the transformation from Se NWs to Ag_2Se NWs (Jiang et al. 2020). EDS mapping (Fig. S2(d)–(f)) proves that Ag and Se elements are uniformly distributed in the Ag_2Se NWs. The EDS spectra (Fig. S2(g)) and element composition table (Fig. S2(h)) confirm that Ag and Se are the main elements of Ag_2Se NWs, with the ratio of Ag to Se is about 2:1. It is consistent with the atomic ratio in the Ag_2Se chemical formula. In Fig. 2(d), all diffraction peaks corresponding to the orthorhombic structure of Ag_2Se (JCPDS 24–1041), with no diffraction peaks of hexagonal phase Se observed, indicating that Se NWs were completely transformed into Ag_2Se NWs with good crystallinity during the reaction (Wang et al. 2023). The diameter of Se NWs synthesized in this study is approximately 150 nm, and the crystal phase is orthorhombic of Ag_2Se NWs, which is consistent with previous reports in the literature (Gates et al. 2002).

XPS was performed to further confirm the successful synthesis and chemical composition of Ag_2Se NWs. Figure S3 shows the Ag, Se, C, and O elements in the

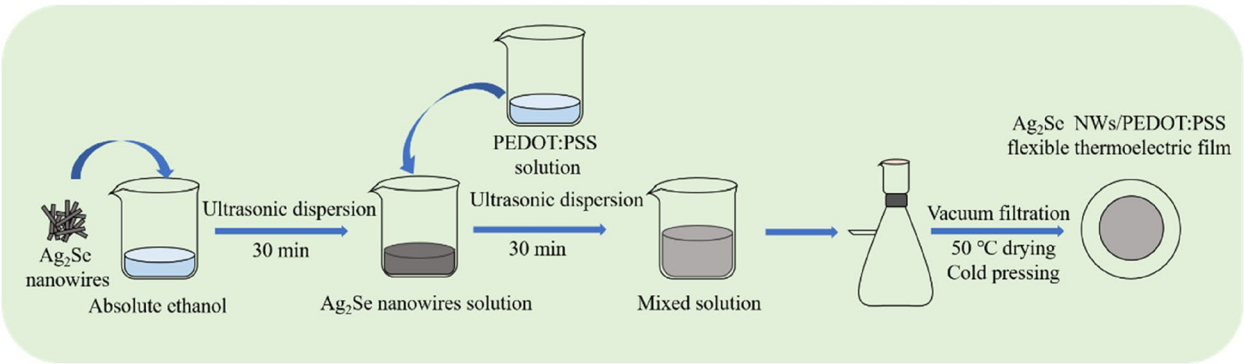

Fig. 1 The fabrication process of Ag_2Se NWs/PEDOT:PSS composite films

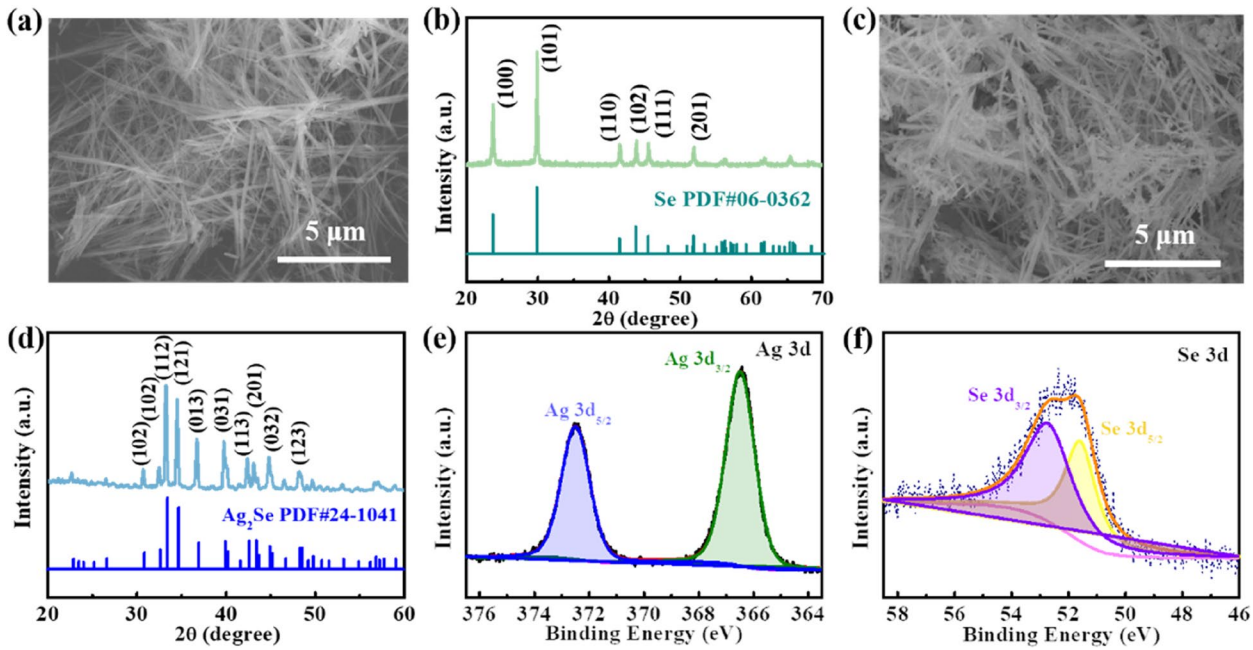

Fig. 2 Structural characterization of Se NWs and Ag_2Se NWs. **a** The surface SEM image of Se NWs. **b** XRD pattern of Se NWs. **c** The surface SEM image of Ag_2Se NWs. **d** XRD pattern of Ag_2Se NWs. **e**, **f** XPS fine spectra of Ag 3d and Se 3d in Ag_2Se NWs, respectively

XPS survey spectra. Figure 2(e, f) displays the fine XPS spectra of Ag 3d and Se 3d, respectively. The peaks at 372.3 and 366.3 eV correspond to the binding energy of Ag $3d_{5/2}$ and Ag $3d_{3/2}$, respectively, which indicates the existence of Ag^+ (Lu et al. 2020). The energy difference between the two peaks is 6.0 eV, which is consistent with the binding energy spectra of Ag 3d electrons in Ag_2Se (Yang et al. 2022). The fitting peaks at approximately 52.5 and 51.4 eV correspond to the binding energy of Se $3d_{3/2}$ and Se $3d_{5/2}$, respectively, indicating that the valence state of Se in the sample is − 2 (Santhosh et al. 2022). The results of XPS and EDS can mutually testify that Ag_2Se NWs are successfully synthesized.

The Ag_2Se NWs/PEDOT:PSS composites were prepared by an ultrasonic-assisted mixing process. SEM surface images of composites before and after cold pressing are shown in Fig. S4–S5. Before cold pressing, the surface morphology of composites is loose with a large number of holes and gaps. After cold pressing, the surface morphology is compact and smooth. According to the SEM cross-section of the composite before and after cold pressing (Fig. S6–S7), the thickness of the composite films after cold pressing is 3.5 ± 1.0 μm, which is much smaller than that of before cold pressing. As shown in Fig. 3(a–d), S, Ag, and Se are the main characteristic elements and they are uniformly dispersed in the composites. The XRD patterns of PEDOT:PSS, AP0, and AP6 are shown in Fig. 3(e). The bulging peaks appearing at 2θ = 25.6° represent the characteristic peaks of the amorphous nature of PEDOT:PSS (Wang et al. 2018), whereas the characteristic XRD peaks for PEDOT:PSS were not detected in AP6 owing to the amorphous characteristics and low content (Lu et al. 2019). The XRD patterns of AP6 and AP0 were almost identical, proving that adding PEDOT:PSS did not change the crystal structure of Ag_2Se. Furthermore, to investigate the effect of cold pressing on the crystal structure of the composites, the XRD pattern of samples before and after cold pressing is shown in Fig. S8. The positions of diffraction peaks before and after cold pressing are consistent, which proves that cold pressing does not change the crystal structure of the composites. However, after cold pressing, the signal-to-noise ratio of the XRD pattern of the composite is improved to some extent, which proves that cold pressing is positive in improving the degree of crystallization of composite materials. Figure S9 shows the Raman spectra of PEDOT:PSS, AP0, and AP6. The peak at 233 cm^{-1} is the symmetric telescopic vibration peak of the Ag-Se bond (Pandiaraman and Soundararajan 2012; Naumov et al. 2016; Zhang et al. 2021c). The peak at 1370 cm^{-1} is corresponding to C_β-C_β telescopic vibration peak of PEDOT. The peaks at 1433 and 1516 cm^{-1} are the C = C symmetric and asymmetric telescopic vibrational peaks (Park et al. 2014). The characteristic peaks of Ag_2Se and PEDOT:PSS were detected simultaneously in the Raman spectra of AP6, which further demonstrates

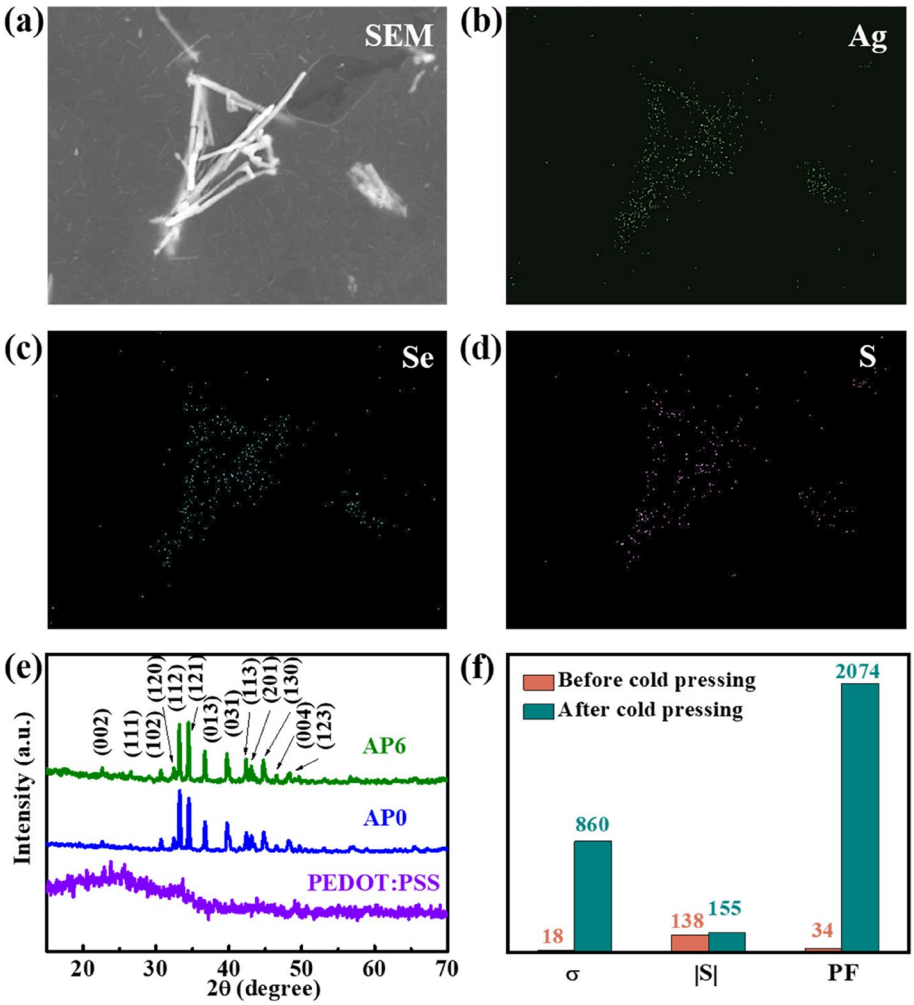

Fig. 3 The fundamental characterization of Ag_2Se NWs/PEDOT:PSS composites. **a**–**d** EDS mapping of S, Se, and Ag elements in composites. **e** XRD patterns of PEDOT:PSS, AP0, and AP6. **f** Seebeck coefficient, conductivity, and power factor of AP6 before and after cold pressing, the unit for σ, |S|, and PF are S cm^{-1}, μV K^{-1}, and μW m^{-1} K^{-2}, respectively

the successful preparation of Ag_2Se NWs/PEDOT:PSS composites. As shown in the inset of Fig. S9, the peaks at 1433 cm^{-1} in PEDOT:PSS shift to 1429 cm^{-1} in AP6. Current research indicates that there may be a templating effect at the organic/inorganic interface accompanied by charge transfer induced de-doping of conductive polymers at the interface (Kumar et al. 2018). Therefore, the molecular chain structure of PEDOT:PSS changes from the coiled benzene to the linear quinone, which leads to the red shift of Raman peaks.

Cold pressing can effectively reduce the contact resistance of the inorganic nanowires inside the composites, which facilitates carrier transport and favors the improvement of thermoelectric properties (Wang et al. 2021a). The thermoelectric properties of the composites before and after cold pressing were measured, respectively, as shown in Fig. 3(f). The comparative properties of the other composites are shown in Fig. S10. It can be seen that cold pressing can improve the conductivity, Seebeck coefficient, and power factor of the composites to a certain extent. The conductivity increases about 47 times from 18.0 to 859.6 S cm^{-1} after cold pressing, and the power factor increases about 61 times from 34.0 to 2074.0 μW m^{-1} K^{-2} after cold pressing.

Figure 4(a) shows that conductivity, Seebeck coefficient, and power factor of the composites firstly increased and then decreased with increasing PEDOT:PSS content. The composites have the maximum power factor of 2074.0 μW m^{-1} K^{-2} at AP6, which has greater advantages than other composite films have been reported (Park et al. 2020, 2021b, 2022) (Table 1). The results of the Hall measurement are shown in Fig. S11. With increasing the content of PEDOT:PSS, the carrier mobility of the composites gradually decreases

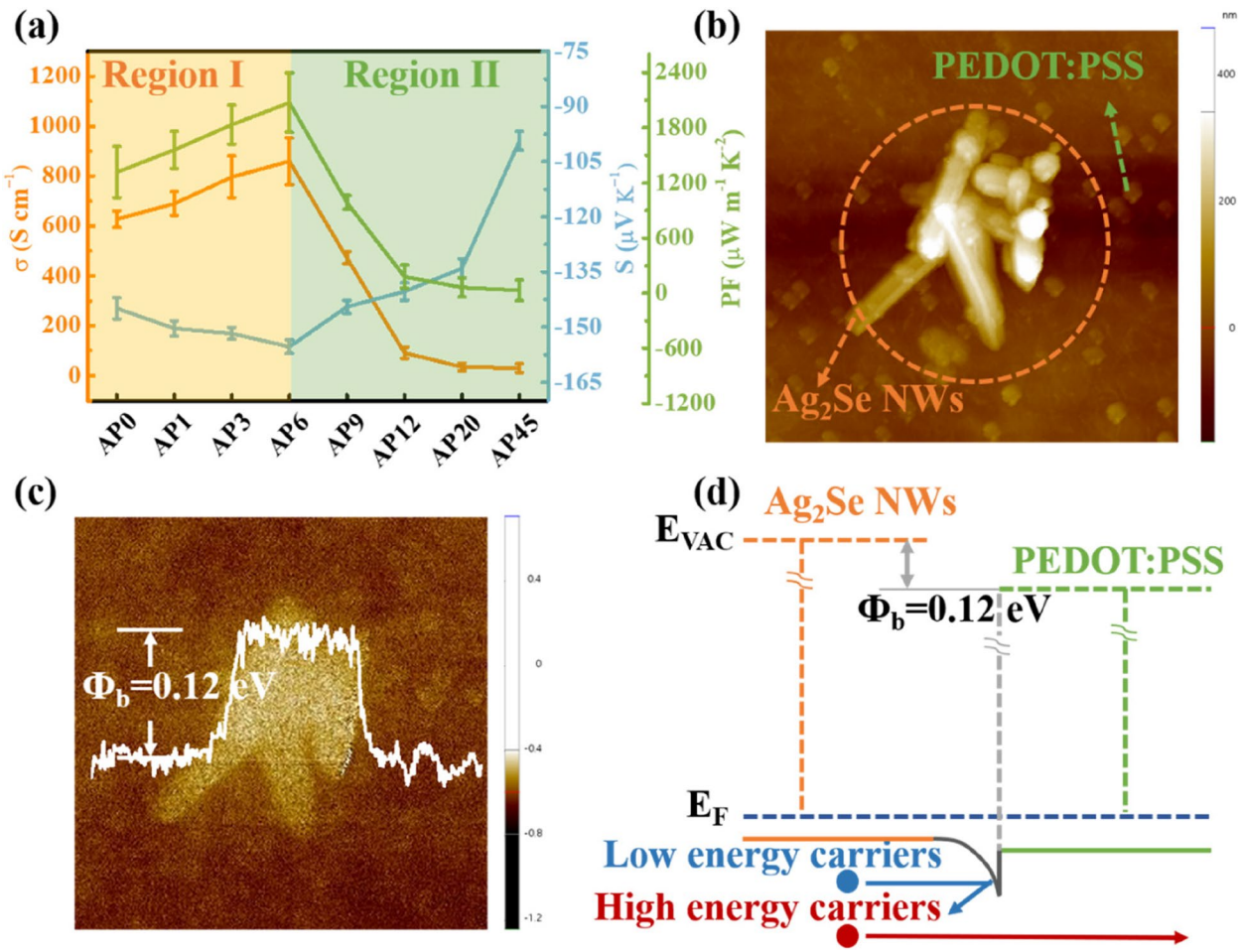

Fig. 4 Thermoelectric properties and interaction characterization of Ag_2Se NWs/PEDOT:PSS composite films. **a** Conductivity, Seebeck coefficient, and power factor of Ag_2Se NWs/PEDOT:PSS composite films with different PEDOT:PSS content. **b** KPFM morphology image of Ag_2Se NWs and PEDOT:PSS. **c** KPFM work function image of Ag_2Se NWs and PEDOT:PSS. **d** Schematic diagram of the energy filtering effect of Ag_2Se NWs/PEDOT:PSS composites

Table 1 The comparison of thermoelectric performance at room temperature with the results reported in the literature

Materials	σ/S cm^{-1}	S/μV K^{-1}	PF/μW m^{-1} K^{-2}	Ref
Ag_2Se/PVP	928.7	−143.4	1910	Liu et al. 2021b)
Ag_2Se/Ag/PEDOT	5957.3	−49.2	1442.5	Wang et al. 2021b)
Ag_2Se/Se/PPy	1064	−144	2240	Li et al. 2022)
Ag_2Se NWs/PEDOT:PSS	520	−91	430	Park et al. 2022)
Ag_2Se NWs/PEDOT:PSS	–-	−51.98	178.59	Park et al. 2020)
Ag_2Se NWs/PEDOT:PSS	–-	–-	327.15	Park et al. 2021b)
Ag_2Se NWs/PEDOT:PSS	859.6	−155.3	2074.0	This work

and the carrier concentration gradually increases, which makes the σ reach the maximum at AP6 due to the relation of $\sigma = ne\mu$ (Li et al. 2024). The typical AFM surface morphology of Ag_2Se NWs and PEDOT:PSS can be clearly observed in the bright and dark regions, respectively (Fig. 4(b)). The work function difference between Ag_2Se NWs and PEDOT:PSS is about 0.12 eV measured by KPFM (Fig. 4(c)), which can achieve an effective energy filtering effect (Gayner and Amouyal 2020). Figure 4(d) shows a schematic diagram of the

energy filtering effect. The low-energy carriers can be scattered by energy barriers, and the high-energy carriers can pass through without any obstruction. The average energy of carriers is increased, which leads to an increase in the Seebeck coefficient (Du et al. 2014).

A single leg (10 mm × 5 mm × 3.5 μm) flexible thermoelectric device was prepared based on AP6. The thermoelectric leg was pasted on the PI tape and coated with conductive silver adhesive on both ends of the leg, and the copper wire was connected to the thermoelectric leg by silver adhesive as an electrode for device performance testing. The schematic diagram of device performance testing is shown in Fig. S12. The output voltage is inversely proportional to the output current (Fig. 5(a)), and the output power (P) is calculated by the following equation:

$$P = U \times I = \frac{U^2}{R_L + R_{\text{in}}} \tag{1}$$

where R_L is the load resistance in the loop and R_{in} is the internal resistance including the resistance of the device R_1 and the contact resistance of the device with the electrode is R_2, the maximum output power is obtained when $R_L = R_{in}$. Figure 5(b) shows the relationship between the output power and load resistance of the device at different temperature differences. The power density of the device at different temperature differences is shown in Fig. 5(c). At ΔT of 25 K, the maximum output power (P_{max}) is about 49.42 nW (20.6 μA, 2.40 mV), corresponding to a load resistance of 108.95 Ω. By dividing by the cross-sectional area of the heat flow, the maximum output power density (PD_{max}) is 4.28 W m^{-2} at ΔT of

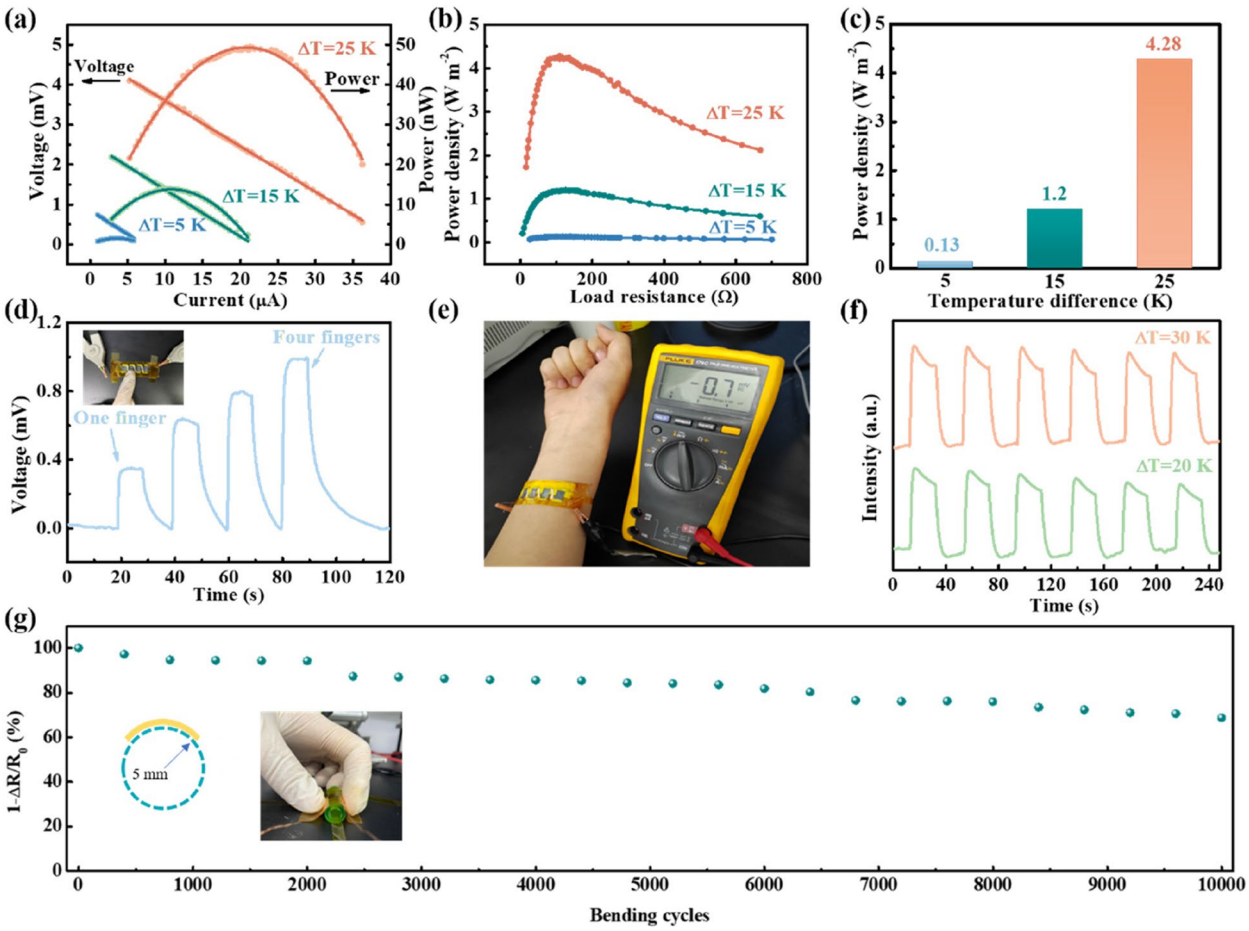

Fig. 5 Output performance of single-leg thermoelectric devices: **a** output voltage and output power versus current at ΔT of 5, 15, and 25 K. **b** The power density versus load resistance at ΔT of 5, 15, and 25 K. **c** The maximum power densities at ΔT of 5, 15, and 25 K. **d** The voltage response curve of four legs thermoelectric devices applied to recognize a different number of fingers. **e** A photo of voltage generations with the human wrist as a thermal source for a four-leg thermoelectric device. **f** The cyclic stability test of the four-leg device at ΔT of 20 and 30 K. **g** The change in resistance of the sample with the bending cycles of 10,000 cycles with the radius of 5 mm, where R and R_0 are the resistance of the bend and flat samples, respectively

25 K, which indicates that the device has a good output performance.

To demonstrate the application of the composite film, a thermoelectric device consisting of four legs was prepared, as shown in Fig. 5(d). When different fingers are placed on the thermoelectric legs of the device, the response of the device to different numbers of fingers is significantly different, showing the device has a good application for temperature sensors. In addition, the thermoelectric device was placed on human skin for energy harvesting (Fig. 5(e)). At the end of the device, dust-free papers were used to isolate the temperature transfer between the device and the skin. An output potential of 0.7 mV could be achieved, which indicates that the device also has a good application in the field of energy harvesting. Subsequently, the cyclic stability of the device was carried out at temperature differences of 20 and 30 K, respectively (Fig. 5(f)). The output voltage of the device did not change significantly after at least six cycles, which proves that the device has a cyclic good stability and can be used stably.

Mechanical property is another significant parameter to assess the performance of flexible thermoelectric devices. The flexibility of single-leg thermoelectric devices was tested as shown in Fig. 5(g). The performance remains at the initial of 94.3% with a radius of 5 mm after 2000 bending cycles. As shown in Fig. S12 (a) and (b), before adding PEDOT:PSS, the retention rate of Seebeck coefficient (S) fluctuates in the range of 82.0–107.2% with the increase of the number of bending cycles within the bending radius of $r = 3$–7 mm. The retention rate of S fluctuated in the range of 82.3–105.7% after adding PEDOT:PSS. As shown in Fig. S13 (c) and (d), before adding PEDOT:PSS, the retention rate of resistance of the film (R) gradually decreased with the increase of the times of bending cycles within the bending radius of $r = 3$–7 mm, and the minimum value of retention rate of R was about 40.0%. However, the retention rate of R remains above 86.0% after adding PEDOT:PSS. The performance comparison of S and R changes before and after adding PEDOT:PSS is shown that the performance of S and R of the sample are optimized after adding PEDOT:PSS, and PEDOT:PSS plays an important role in improving the flexibility of the composite. In addition, the flexibility of the device was further tested for 10,000 bending cycles, and the performance of the device remained 70% of the original. Compared with literatures, the device in this paper has good mechanical properties (Li et al. 2022; Lu et al. 2020; Park et al. 2021b; Wang et al. 2021b; Hu et al. 2023) (Table 2).

Table 2 The comparison of flexibility performances with the results reported in the literature

Materials	r/mm	Bent times	1-$\Delta R/R_0$ (%)	Ref
Ag_2Se/Ag/PEDOT	4	1500	92.3	Wang et al. 2021b)
Ag_2Se/Se/PPy	4	2000	88.4	Li et al. 2022)
PEDOT/Ag_2Se/CuAgSe	4	1600	84	Lu et al. 2020)
SWCNT/Ag_2Se	5	1000	95	Hu et al. 2023)
Ag_2Se NWs/PEDOT:PSS	–	1000	94.1	Park et al. 2021b)
Ag_2Se NWs/PEDOT:PSS	5	2000 10,000	94.3 70	This work

Conclusions

In this work, the high-performance Ag_2Se NWs/PEDOT:PSS composites were fabricated by physic mixing. When the content of PEDOT:PSS is 1.54 wt%, the composite film obtained the maximum power factor of ~ 2074.0 μW m^{-1} K^{-2} at room temperature. The thermoelectric device based on the composite film has good output performance with the P_{max} of ~ 49.42 nW and the PD_{max} of ~ 4.28 W m^{-2} at ΔT of 25 K. The device also has good mechanical properties with remaining the initial of 94.3% after 2000 bending cycles with a radius of 5 mm. This work provides good guidance for improving the thermoelectric properties of composites and designing and preparing high-performance flexible composite thermoelectric devices.

Supplementary Information

The online version contains supplementary material available at https://doi.org/10.1186/s40712-025-00235-6.

Additional file 1: Fig. S1 The preparation process diagram of Se NWs and Ag_2Se NWs. Fig. S2 (a) The SEM image of Se NWs. (b) EDS mapping of Se in Se NWs. (c) EDS spectra of element distribution in Se NWs. (d)-(f) The SEM image and EDS mapping of Ag and Se in Ag_2Se NWs. (g) EDS spectra of element distribution in Ag_2Se NWs. (h) Element composition table of Ag_2Se NWs. Fig. S3 XPS survey spectra of Ag_2Se NWs. Fig. S4 (a)-(h) The SEM images of AP0, AP1, AP3, AP6, AP9, AP12, AP20 and AP45 before cold pressing, respectively. Fig. S5 (a)-(h) The SEM images of AP0, AP1, AP3, AP6, AP9, AP12, AP20 and AP45 after cold pressing, respectively. The inset images of (f)-(h) are high magnification SEM. Fig. S6 (a)-(h) The cross-section SEM images of AP0, AP1, AP3, AP6, AP9, AP12, AP20 and AP45 before cold pressing, respectively. Fig. S7 (a)-(h) The cross-section SEM images of AP0, AP1, AP3, AP6, AP9, AP12, AP20 and AP45 after cold pressing, respectively. Fig. S8 XRD patterns of AP6 before and after cold pressing. Fig.S9 Raman spectra of PEDOT:PSS, AP0 and AP6. The inset is partial enlarged detail of peak at 1433 cm^{-1}. Fig. S10 (a) Conductivity, (b) Seebeck coefficient, and (c) power factor of samples before and after cold pressing, respectively. Fig. S11 Hall measurement of Ag_2Se NWs/PEDOT:PSS composites, (a) carrier mobility and (b) carrier concentration. Fig. S12 Schematic diagram of output performance test of thermoelectric devices. Fig. S13 The retention rate curve of S (a) before adding PEDOT:PSS and (b) after adding PEDOT:PSS with 2000 bending cycles under different bending radii with r = 3, 4, 5, 6 and 7 mm, respectively. The retention rate

curve of R (c) before adding PEDOT:PSS and (d) after adding PEDOT:PSS with 2000 bending cycles under different bending radii with r = 3, 4, 5, 6 and 7 mm, respectively.

Acknowledgements
This work was financially supported by the National Key R&D Program of China (No. 2022YFC3006303).

Data and code availability
All data and code generated or used during the study appear in the submitted article.

Authors' contributions
Ruoxi Wang: data curation, formal analysis, investigation, and writing—original draft. Rongke Sun: formal analysis. Yanmei Ren: methodology. Yanqing Ma: funding acquisition, validation, and writing—review and editing, and supervision. Lei Ma: funding acquisition, conceived and supervised the whole project, methodology, conceptualization, writing—review and editing, and supervision.

Data availability
Supplementary information including measurements for characterization (XRD, SEM, Raman of the different shape samples), supporting tables, conductivity, and Seebeck coefficient results.

Declarations

Ethics approval and consent to participate
There are no experiments involving human tissue in this article.

Competing interests
The authors declare that they have no known competing financial interests or personal relationships that could have appeared to influence the work reported in this paper.

Received: 31 July 2024 Accepted: 6 February 2025
Published online: 26 February 2025

References

Ding Y, Qiu Y, Cai K, Yao Q, Chen S, Chen L, He J (2019) High performance n-type Ag_2Se film on nylon membrane for flexible thermoelectric power generator. Nat Commun 10(1):841
Du Y, Cai KF, Chen S, Cizek P, Lin T (2014) Facile preparation and thermoelectric properties of Bi_2Te_3 based alloy nanosheet/PEDOT:PSS composite films. ACS Appl Mater Interfaces 6(8):5735–5743
Gates B, Mayers B, Wu Y, Sun Y, Cattle B, Yang P, Xia Y (2002) Synthesis and characterization of crystalline Ag_2Se nanowires through a template-engaged reaction at room temperature. Adv Func Mater 12(10):679–686
Gayner C, Amouyal Y (2020) Energy filtering of charge carriers: current trends, challenges, and prospects for thermoelectric materials. Adv Func Mater 30(18):1901789
Goo G, Anoop G, Unithrattil S, Kim WS, Lee HJ, Kim HB, Jung M-H, Park J, Ko HC, Jo JY (2019) Proton-irradiation effects on the thermoelectric properties of flexible Bi_2Te_3/PEDOT:PSS composite films. Adv Electron Mater 5(4):1800786
Hu Q-X, Liu W-D, Zhang L, Sun W, Gao H, Shi X-L, Yang Y-L, Liu Q, Chen Z-G (2023) SWCNTs/Ag_2Se film with superior bending resistance and enhanced thermoelectric performance via in situ compositing. Chem Eng J 457:141024
Hu Q-X, Liu W-D, Zhang L, Gao H, Wang D-Z, Wu T, Shi X-L, Li M, Liu Q-F, Yang Y-L, Chen Z-G (2024) Carrier separation boosts thermoelectric performance of flexible n-type Ag_2Se-based films. Adv Energy Mater 14(36):2401890
Huang X, Liu Y, Zhou J, Nejad SK, Wong TH, Huang Y, Li H, Yiu CK, Park W, Li J, Su J, Zhao L, Yao K, Wu M, Gao Z, Li D, Li J, Shi R, Yu X (2022) Garment embedded sweat-activated batteries in wearable electronics for continuous sweat monitoring. npj Flexible Electron 6(1):10
Jiang C, Ding Y, Cai K, Tong L, Lu Y, Zhao W, Wei P (2020) Ultrahigh performance of n-type Ag_2Se films for flexible thermoelectric power generators. ACS Appl Mater Interfaces 12(8):9646–9655
Kumar P, Zaia EW, Yildirim E, Repaka DM, Yang S-W, Urban JJ, Hippalgaonkar KJNC (2018) Polymer morphology and interfacial charge transfer dominate over energy-dependent scattering in organic-inorganic thermoelectrics. Nat Commun 9(1):5347
Li Q, Yam VW-W (2006) High-yield synthesis of selenium nanowires in water at room temperature. Chem Commun 9:1006–1008
Li Y, Lou Q, Yang J, Cai K, Liu Y, Lu Y, Qiu Y, Lu Y, Wang Z, Wu M, He J, Shen S (2022) Exceptionally high power factor Ag_2Se/Se/polypyrrole composite films for flexible thermoelectric generators. Adv Func Mater 32(7):2106902
Li S, Chen T, Wang Z, Danish MH, Yao G, Chen K, Ge Z, Li D, Xin H, Zhang J, Qin X (2024) Improved thermoelectric performance of n-type BiTeSe based composites incorporated with PEDOT: PSS polymer nanoinclusions. Mater Today Chem 37:102008
Liu C, Shan D-L, Shen Z-H, Ren G-K, Yue W, Zhou Z-F, Li J-Y, Yi D, Lan J-L, Chen L-Q, Snyder GJ, Lin Y-H, Nan C-W (2021) Role of interfaces in organic–inorganic flexible thermoelectrics. Nano Energy 89:106380.
Liu YF, Liu PP, Jiang QL, Jiang F, Liu J, Liu G, Liu C, Du Y, Xu J (2021b) Organic/inorganic hybrid for flexible thermoelectric fibers. Chem Eng J 405:126510
Liu Y, Wang X, Hou S, Wu Z, Wang J, Mao J, Zhang Q, Liu Z, Cao F (2023) Scalable-produced 3D elastic thermoelectric network for body heat harvesting. Nat Commun 14(1):3058
Lu Y, Ding Y, Qiu Y, Cai K, Yao Q, Song H, Tong L, He J, Chen L (2019) Good performance and flexible PEDOT:PSS/Cu_2Se nanowire thermoelectric composite films. ACS Appl Mater Interfaces 11(13):12819–12829
Lu Y, Qiu Y, Cai K, Li X, Gao M, Jiang C, He J (2020) Ultrahigh performance PEDOT/Ag_2Se/CuAgSe composite film for wearable thermoelectric power generators. Mater Today Phys 14:100223
Lu Y, Han X, Wei P, Liu Y, Wang Z, Zuo X, Zhao W, Cai K (2024) Nanoengineering approach toward ultrahigh power factor Ag_2Se/polyvinylpyrrolidone composite film for flexible thermoelectric generator. Chem Eng J 485:149793
Meng Q, Yin S, Qin J, Ma S, Wang L (2024) PEDOT:PSS functionalized silver selenide composite films for thermoelectric applications. ACS Appl Nano Mater 7(20):23513–23518
Naumov P, Barkalov O, Mirhosseini H, Felser C, Medvedev SA (2016) Atomic and electronic structures evolution of the narrow band gap semiconductor Ag_2Se under high pressure. J Phys: Condens Matter 28(38):385801
Pandiaraman M, Soundararajan N (2012) Micro-Raman studies on thermally evaporated Ag_2Se thin films. J Theoret Appl Phys 6(1):7
Park H, Lee SH, Kim FS, Choi HH, Cheong IW, Kim JH (2014) Enhanced thermoelectric properties of PEDOT:PSS nanofilms by a chemical dedoping process. J Mater Chem A 2(18):6532–6539
Park D, Kim M, Kim J (2020) Fabrication of PEDOT: PSS/Ag_2Se nanowires for polymer-based thermoelectric applications. Polymers 12(12):2932
Park D, Ju H, Kim J (2021a) Enhanced thermoelectric properties of flexible N-type Ag_2Se nanowire/polyvinylidene fluoride composite films synthesized via solution mixing. J Ind Eng Chem 93:333–338
Park D, Kim M, Kim J (2021b) Conductive PEDOT: PSS-based organic/inorganic flexible thermoelectric films and power generators. Polymers 13(2):210
Park D, Lee S, Kim JJCC (2022) Thermoelectric and mechanical properties of PEDOT: PSS-coated Ag_2Se nanowire composite fabricated via digital light processing based 3D printing. Composites Commun 30:101084
Ren Y, Sun R, Yu X, Wang R, Zhang W, Zhu X, Ma Y, Ma L (2023) A systematic study on synthesis parameters and thermoelectric properties of tellurium nanowire bundles. Mater Adv 4(19):4455–4462
Santhosh R, Abinaya R, Archana J, Ponnusamy S, Harish S, Navaneethan M (2022) Controlled grain boundary interfaces of reduced graphene oxide in Ag_2Se matrix for low lattice thermal conductivity and enhanced power factor for thermoelectric applications. J Power Sources 525:231045
Shi XL, Zou J, Chen ZG (2020) Advanced thermoelectric design: from materials and structures to devices. Chem Rev 120(15):7399–7515
Sun Q, Wang L, Ren G, Zhang L, Sheng H, Zhu Y, Wang H, Lu G, Yu H-D, Huang W (2022) Smart band-aid: multifunctional and wearable electronic device

for self-powered motion monitoring and human-machine interaction. Nano Energy 92:106840
Wang X, Kyaw AKK, Yin C, Wang F, Zhu Q, Tang T, Yee PI, Xu J (2018) Enhancement of thermoelectric performance of PEDOT:PSS films by post-treatment with a superacid. RSC Adv 8(33):18334–18340
Wang Y, Yang L, Shi X-L, Shi X, Chen L, Dargusch MS, Zou J, Chen Z-G (2019) Flexible thermoelectric materials and generators: challenges and innovations. Adv Mater 31(29):1807916
Wang W, Sun Y, Feng Y, Qin H, Zhu J, Guo F, Cai W, Sui JJMTP (2021) High thermoelectric performance bismuth telluride prepared by cold pressing and annealing facilitating large scale application. Mater Today Phys 21:100522
Wang Z, Gao Q, Wang W, Lu Y, Cai K, Li Y, Wu M, He J (2021b) High performance Ag_2Se/Ag/PEDOT composite films for wearable thermoelectric power generators. Materials Today Physics 21:100553
Wang Z, Liu Y, Li J, Huang C, Cai K (2023) High-performance Ag_2Se film by a template method for flexible thermoelectric generator. Mater Today Phys 36:101147
Xu K, Lu Y, Takei K (2019) Multifunctional skin-inspired flexible sensor systems for wearable electronics. Adv Mater Technol 4(3):1800628
Yang S, Zhang H, Zhang J, Zhou X (2022) A novel route for preparing Ag_2Se-based micro-nanocomposites and their photocatalytic activity. J Nanopart Res 24(8):170
Yang D, Shi X-L, Li M, Nisar M, Mansoor A, Chen S, Chen Y, Li F, Ma H, Liang GX, Zhang X, Liu W, Fan P, Zheng Z, Chen Z-G (2024) Flexible power generators by Ag_2Se thin films with record-high thermoelectric performance. Nat Commun 15(1):923
Zhang L, Shi X-L, Yang Y-L, Chen Z-G (2021a) Flexible thermoelectric materials and devices: from materials to applications. Mater Today 46:62–108
Zhang X, Pan S, Song H, Guo W, Zhao S, Chen G, Zhang Q, Jin H, Zhang L, Chen Y (2021b) Polymer–inorganic thermoelectric nanomaterials: electrical properties, interfacial chemistry engineering, and devices. Front Chem 9:677821
Zhang D, Wu R, Cao R, Xu S (2021c) One-step hydrothermal synthesis of Ag_2Se/amorphous MoSex heterojunction with enhanced visible-light photocatalytic degradation performance. Mater Lett 300:130218
Zhou H, Chua MH, Zhu Q, Xu J (2021) High-performance PEDOT:PSS-based thermoelectric composites. Compos Commun 27:100877

Publisher's Note